QCD phase diagram and equation of state in background electric fields

G. Endrődi and G. Markó
Fakultät für Physik, Universität Bielefeld, D-33615 Bielefeld, Germany

(Received 22 September 2023; accepted 23 January 2024; published 8 February 2024)

The phase diagram and the equation of state of quantum chromodynamics (QCD) is investigated in the presence of weak background electric fields by means of continuum extrapolated lattice simulations. The complex action problem at nonzero electric field is circumvented by a novel Taylor expansion, enabling the determination of the linear response of the thermal QCD medium to constant electric fields—in contrast to simulations at imaginary electric fields, which, as we demonstrate, involve an infrared singularity. Besides the electric susceptibility of QCD matter, we determine the dependence of the Polyakov loop on the field strength to leading order. Our results indicate a plasma-type behavior with a negative susceptibility at all temperatures, as well as an increase in the transition temperature as the electric field grows.

DOI: 10.1103/PhysRevD.109.034506

I. INTRODUCTION

The phase structure of quantum chromodynamics (QCD) in the presence of background electromagnetic fields is an essential attribute of the fundamental theory of quarks and gluons and, accordingly, a subject of active theoretical research. The electromagnetic response of the QCD medium is relevant for a range of physical situations, e.g., the phenomenology of heavy-ion collisions, the description of neutron star interiors or the evolution of our universe in its early stages, see the reviews [1,2]. Electric fields have been discussed both in the context of neutron stars (with inhomogeneous cores) [3] as well as for the initial stages of heavy-ion collisions [4,5]. If in these settings the electromagnetic fields are sufficiently long-lived compared to the strong scale (this is a delicate topic for heavy-ion collisions [6–8]), it is appropriate to consider QCD matter in a background magnetic or electric field in equilibrium.

Before equilibration, electric fields E induce a dynamical response via the electrical conductivity of the medium [9]. The subsequently emerging equilibrium necessarily involves—in contrast to the case of magnetic fields B—an inhomogeneous charge distribution $n(x)$ in the thermal medium while having constant temperature T everywhere [10]. The distribution is uniquely fixed by the requirement that pressure gradients and electric forces cancel each other and thus no currents flow [11]. The equilibrium system is therefore described by a *local canonical* statistical ensemble, where $n(x)$ is held fixed. It differs from the grand canonical ensemble parametrized by chemical potentials, employed usually at $E = 0$. This aspect renders comparisons between equilibrium systems at $E > 0$ and $E = 0$, e.g., by means of lattice simulations, problematic.

Moreover, the proper definition of the equilibrium state at $E > 0$ requires infrared regularization (e.g., a finite spatial volume V) that prevents charges to be accelerated to infinity. As we have demonstrated recently within perturbative QED [12], the $E \to 0$ and $V \to \infty$ limits of this setup do not commute at nonzero temperature. This renders approaches based on Schwinger's exact $E > 0$ infinite-volume propagator [13] and infrared-regularized weak-field expansions in the manner of Weldon [14] inherently different. For a certain physical setting, the boundary conditions determine which is the appropriate limit to consider. The generalization of these ideas to the case of QCD enables one to explore the impact of background electric fields on strongly interacting matter as well as the associated phase diagram: our objectives in the present paper.

The impact of magnetic fields on the QCD crossover [15,16] and the corresponding phase diagram is well understood and has been studied extensively on the lattice [17–22], as well as within models and effective theory approaches (for a recent review, see Ref. [23]). In contrast, electric fields render the QCD action complex, hindering standard lattice simulations. Alternative approaches include Taylor-expansions [24–27], calculations at imaginary electric fields [28–35] and simulations with electric fields that couple to the isospin charge of quarks [36]. Still, there are no existing results for the QCD equation of state nor the phase diagram. The latter has only been studied within effective theories like the linear σ model [37], variants of the Nambu-Jona-Lasinio (NJL) model [38–41] and the

Euler-Heisenberg effective action [42]. These calculations are all based on the Schwinger propagator.

In this paper, we determine the QCD equation of state and the phase diagram on the lattice for the first time for weak background electric fields. The complex action problem is circumvented via a Taylor-expansion: this corresponds to the Weldon-type regularization of the electrically polarized thermal medium and is the proper description of a finite system, where equilibration takes place in the presence of a weak electric field. The expansion is based on the method we developed in Refs. [12,43], and resembles the analogous approach for background magnetic fields [44–46]. Besides the leading coefficient—the electric susceptibility of QCD matter—we also determine the leading series of the Polyakov loop. Using this observable, we construct the phase diagram and demonstrate that the transition temperature increases as E grows—contrary to existing model predictions, e.g., [40]. Finally, we demonstrate that lattice simulations at nonzero imaginary electric fields cannot be used to directly calculate the electric susceptibility due to the singular change of ensembles between $E = 0$ and $iE \neq 0$. Some of our preliminary results have already been presented in Ref. [43].

II. LATTICE SETUP AND OBSERVABLES

QCD matter in thermal equilibrium is a medium that can be polarized by weak background electromagnetic fields. The associated static linear response is characterized by the electric and magnetic susceptibilities (we employ the same notation as in Ref. [12]). These are defined via the matter free energy density f,

$$\xi_b = -\frac{\mathrm{d}^2 f}{\mathrm{d}(eE)^2}\bigg|_{E=0}, \qquad \chi_b = -\frac{\mathrm{d}^2 f}{\mathrm{d}(eB)^2}\bigg|_{B=0}. \tag{1}$$

Here, the subscript b indicates that both susceptibilities contain ultraviolet divergent terms that must be subtracted via additive renormalization, see below. The elementary charge e is included so that we can work with the renormalization group invariants eE and eB.

The matter free energy density can be rewritten using the partition function $\mathcal{Z}$ of the system. Using the rooted staggered formalism of lattice QCD, it is given by the Euclidean path integral over the gluon links U,

$$\mathcal{Z} = \int \mathcal{D}U e^{-\beta S_g} \prod_f \det[\not{D}(q_f) + m_f]^{1/4}, \tag{2}$$

where $\beta = 6/g^2$ is the inverse gauge coupling and m_f denotes the quark masses with $f = u, d, s$ running over the quark flavors. We use a periodic spatial volume $V = L^3$ with linear size L. Note that $\mathcal{Z}$ corresponds to the grand canonical ensemble; its relation to the canonical one at $E > 0$ is discussed in Sec. II B. In Eq. (2), S_g is the gluon action (in our discretization, the tree-level improved Symanzik action) and $\not{D}_f$ is the staggered Dirac operator (including a twofold stout smearing of the links) that contains the quark charges $q_u/2 = -q_d = -q_s = e/3$. The quark masses are set to their physical values as a function of the lattice spacing a [47]. Further details of the action and of our simulation algorithm are given in Refs. [18,48].

We choose a gauge for the background electromagnetic field A_ν, where $A_0(x_1)$ represents the electric field (pointing in the x_1 direction) and $A_2(x_1)$ the magnetic field (in the x_3 direction). While magnetic fields are identical in Minkowski and Euclidean space-times, the vector potential relevant for the electric field undergoes a Wick rotation so that $A_4 = iA_0$. This is similar to the case of a (real) charge chemical potential μ, corresponding to a homogeneous A_0 field. In the path integral (2), A_ν enters the Dirac operator in the form of parallel transporters $u_{\nu,f} = \exp(iaq_f A_\nu)$ multiplying the gluon links U_ν with $1 \leq \nu \leq 4$. In the case of imaginary electric fields and imaginary chemical potentials the parallel transporters again take the form of phases, and their effect will be separately discussed in Sec. III C. Finally we mention that in our setup, the electromagnetic field is not dynamical, i.e. quarks do not interact with each other via photons but only couple to the background gauge field. The independent thermodynamic variable is the field E that enters the Dirac operator, analogously to the situation for magnetic fields [49].

A. Susceptibility

As we demonstrated in Ref. [12], the susceptibilities of Eq. (1) are related to derivatives of the electromagnetic vacuum polarization tensor with respect to spatial momenta. For our gauge choice, these relations read in terms the Euclidean polarization tensor $\Pi_{\mu\nu}$,

$$\xi_b = -\frac{1}{2}\frac{\partial^2 \Pi_{44}(k)}{\partial k_1^2}\bigg|_{k=0}, \qquad \chi_b = \frac{1}{2}\frac{\partial^2 \Pi_{22}(k)}{\partial k_1^2}\bigg|_{k=0}, \tag{3}$$

with a spatial momentum $k = (k_1, 0, 0, 0)$. In other words, the zero momentum limit is considered at vanishing timelike frequency, reflecting the static nature of the susceptibilities. The negative sign for ξ_b in (3) appears due to the Wick rotation of the electric field. We highlight that the equilibrium systems at different values of E exhibit different charge profiles $n(x_1)$, and this implicit E-dependence is taken into account properly in Eq. (3) for the calculation of ξ_b [12]. In fact, without this contribution, ξ_b would diverge in the $k_1 \to 0$ limit.

The vacuum polarization tensor is defined as the correlator

$$\Pi_{\mu\nu}(k) = \int \mathrm{d}^4 x e^{ikx} \langle j_\mu(x) j_\nu(0) \rangle, \tag{4}$$

of the electromagnetic current $j_\mu = \sum_f \frac{q_f}{e} \bar{\psi}_f \gamma_\mu \psi_f$, for which we use the conserved (one-link) staggered vector

current. It is convenient to evaluate (3) in coordinate space, where the bare susceptibilities become [12,43]

$$\xi_b = -\langle G_{44}^{(2)} \rangle, \qquad \chi_b = \langle G_{22}^{(2)} \rangle, \tag{5}$$

containing the second moment of a partially zero-momentum projected two-point function

$$G_{\mu\nu}^{(2)} = \int_0^{L/2} \mathrm{d}x_1 x_1^2 G_{\mu\nu}(x_1), \tag{6}$$

$$G_{\mu\nu}(x_1) = \int \mathrm{d}x_2 \mathrm{d}x_3 \mathrm{d}x_4 j_\mu(x) j_\nu(0). \tag{7}$$

The Grassmann integral over quark fields is understood to be implicitly carried out on the right-hand side of the last equation.

Both susceptibilities undergo additive renormalization. This originates from the multiplicative divergence in the electric charge e [45,50,51]. Being temperature-independent, the divergence cancels in

$$\xi = \xi_b(T) - \xi_b(T=0), \qquad \chi = \chi_b(T) - \chi_b(T=0), \tag{8}$$

which sets $\xi = \chi = 0$ at zero temperature. In fact, at $T = 0$ Lorentz invariance ensures that $\langle G_{22}^{(2)} \rangle = \langle G_{44}^{(2)} \rangle$, implying that the bare magnetic and electric susceptibilities coincide up to a minus sign. To renormalize the electric susceptibility, we can therefore employ the existing results for $\chi_b(T=0)$ from Ref. [45].

B. Polyakov loop and its expansion

Next we consider the bare Polyakov loop operator,

$$P_b = \frac{1}{V} \int \mathrm{d}^3\mathbf{x} \mathrm{ReTr} \prod_{x_4} U_4(x). \tag{9}$$

Its expectation value is related to the free energy of a static, electrically neutral color charge and is often taken as a measure of deconfinement. Just as for ξ_b, the contribution of the equilibrium charge profile needs to be taken into account for the E-dependence of the Polyakov loop as well. As we will show below, the proper second-order expansion of $\langle P_b \rangle$ is given by the correlator

$$\varphi_E^n \equiv \left. \frac{\mathrm{d}^2 \langle P_b \rangle^n}{\mathrm{d}(eE)^2} \right|_{E=0} = \frac{V}{T} \left[-\langle P_b G_{44}^{(2)} \rangle + \langle P_b \rangle \langle G_{44}^{(2)} \rangle \right], \tag{10}$$

where the superscript n on the left denotes that the derivative is evaluated along the equilibrium condition specified by the local charge profiles. Analogously, the magnetic derivative of $\langle P_b \rangle$ can be obtained by replacing $-G_{44}^{(2)}$ by $G_{22}^{(2)}$ in Eq. (10), although in that case nontrivial charge distributions do not appear. The rest of this subsection is devoted to the derivation of Eq. (10).

In the presence of the electric field, the equilibrium charge density profile $n(x_1)$ varies in the x_1 direction (the coordinate system is chosen so that $-L/2 \le x_1 \le L/2$). We now consider the implications of such an equilibrium using a homogeneous background field generated by the vector potential $A_0(x_1) = Ex_1$, regularized by the finite system size (assuming open boundary conditions). Moreover, the field is assumed to be weak so that the system can be thought of as a collection of subsystems with approximately constant density. These are characterized by a canonical ensemble $\langle P_b \rangle^n$ parameterized by the local density, instead of the usual grand canonical ensemble average $\langle P_b \rangle$ parametrized by the charge chemical potential $\bar{\mu}(x_1)$. The two are related by a local Legendre transformation [12],

$$\langle P_b \rangle^n = \frac{1}{L} \int \mathrm{d}x_1 \left[\langle P_b \rangle - \mu \frac{\partial \langle P_b \rangle}{\partial \mu} \right]_{\mu = \bar{\mu}(x_1)}. \tag{11}$$

The local chemical potential is fixed by the requirement that diffusion and electric forces cancel, i.e., $\bar{\mu}(x_1) = -eEx_1$. This choice corresponds to a globally neutral system, where the volume average of the charge chemical potential vanishes.

Taking the second total derivative of (11) with respect to eE, and evaluating it at $E = 0$ (implying $\bar{\mu} = 0$), we obtain for the left-hand side of (10),

$$\varphi_E^n = \frac{1}{L} \int \mathrm{d}x_1 [\varphi_E - \varphi_\mu \cdot x_1^2], \tag{12}$$

with

$$\varphi_E = \left. \frac{\partial^2 \langle P_b \rangle}{\partial (eE)^2} \right|_{E=0}, \qquad \varphi_\mu = \left. \frac{\partial^2 \langle P_b \rangle}{\partial \mu^2} \right|_{\mu=0}. \tag{13}$$

The Polyakov loop operator P_b does not depend explicitly on the electric field nor on the chemical potential. The derivatives of $\langle P_b \rangle$ therefore merely involve the derivative of the weight in the path integral (2).

Let us first discuss φ_μ. The chemical potential multiplies the volume integral of j_4 in the Euclidean action (before integrating out fermions), therefore

$$\varphi_\mu = \int \mathrm{d}^4 y \mathrm{d}^4 z [\langle P_b j_4(y) j_4(z) \rangle - \langle P_b \rangle \langle j_4(y) j_4(z) \rangle], \tag{14}$$

where we used that $\langle j_4(y) \rangle = 0$ due to parity symmetry. Substituting the integration variable z by $u = z - y$, exploiting the translational invariance of the correlators and using the definition (7) of the projected correlator, we arrive at

$$\varphi_\mu = \frac{V}{T}\int \mathrm{d}u_1[\langle P_b G_{44}(u_1)\rangle - \langle P_b\rangle\langle G_{44}(u_1)\rangle]. \quad (15)$$

Next, we turn to φ_E. This time, the Euclidean action contains the four-volume integral of $ieA_4(y_1)\cdot j_4(y_1)$ with $A_4(y_1) = iEy_1$. The second derivative therefore becomes

$$\varphi_E = \int \mathrm{d}^4y\mathrm{d}^4z y_1 z_1[\langle P_b j_4(y) j_4(z)\rangle - \langle P_b\rangle\langle j_4(y) j_4(z)\rangle], \quad (16)$$

We proceed by rewriting $y_1 z_1 = -(z_1 - y_1)^2/2 + (y_1^2 + z_1^2)/2$ and use that the second term can be replaced by y_1^2 as it multiplies a factor that is symmetric under the exchange of y_1 and z_1 under the integrals. With the same variable substitution as above, the use of translational invariance of the correlators this time gives

$$\varphi_E = -\frac{V}{T}\int \mathrm{d}u_1 \frac{u_1^2}{2}[\langle P_b G_{44}(u_1)\rangle - \langle P_b\rangle\langle G_{44}(u_1)\rangle] + \frac{1}{L}\int \mathrm{d}y_1 y_1^2\cdot\varphi_\mu. \quad (17)$$

The second term in (17)—where we recognized φ_μ from Eq. (15)—is clearly divergent in the thermodynamic limit. Coming back to (12), we see that this infrared singular term exactly cancels in φ_E^n, rendering the curvature of the Polyakov loop expectation value finite when evaluated along the equilibrium condition involving the inhomogeneous charge profile. Finally, employing the $u_1 \leftrightarrow -u_1$ symmetry of the $E = 0$ system, we end up with Eq. (10), involving the second moment $G_{44}^{(2)}$ defined in Eq. (6).

Up to this point we considered the bare Polyakov loop, which is subject to multiplicative renormalization [52],

$$P(a,T,E) = P_b(a,T,E)\cdot\left(\frac{P_\star}{P_b(a,T_\star,E=0)}\right)^{T_\star/T}, \quad (18)$$

where the renormalization factor (i.e., the second factor) is independent of the background field and has been determined for our lattice spacings in Ref. [53]. In our renormalization scheme, we fix $\langle P\rangle = 1$ at $T = 162$ MeV and $E = B = 0$. The renormalization point, $T = 162$ MeV approximately coincides with the deconfinement temperature one infers from the strange quark susceptibility at $E = 0$ [54]. We will later use the criterion $\langle P\rangle = 1$ to estimate the transition temperature at $E \neq 0$ as well based on the same notion.

III. RESULTS

We will now report on the measured observables, including some details on the G_{44} correlator, which plays a central role in our method. We also discuss the immediate conclusions one can draw from the behavior of the observables. We start with the susceptibility, then discuss the Polyakov loop and the deconfinement temperature, and finally we comment on simulations carried out in imaginary electric fields.

A. Susceptibility

We have measured the zero-momentum projected density-density correlator $\langle G_{44}\rangle$, defined in (7), for a broad range of temperatures on $N_t = 6$, 8, 10 and 12 lattice ensembles. Each ensemble consists of 100-300 gauge configurations, separated by five hybrid Monte-Carlo trajectories to reduce autocorrelation. We use $\mathcal{O}(1000)$ random sources located on three-dimensional x_1-slices of our lattices for the calculation. We take into account both connected and disconnected contributions in the two-point function. More details regarding the implementation can be found in [44], where the analogous $\langle G_{22}\rangle$ current-current correlator is evaluated for the magnetic susceptibility.

In Fig. 1 we show the zero-momentum projected $\langle G_{44}\rangle$ as a function of the coordinate at $T \approx 176$ MeV. For comparison, the current-current correlator $\langle G_{22}\rangle$, relevant for the magnetic response, is also included. A substantial difference is visible, reflecting the absence of Lorentz symmetry at this high temperature. It is interesting to note the systematic oscillation of $\langle G_{44}(x_1)\rangle$ between even and odd distances—related to the use of staggered fermions—which is however absent for $\langle G_{22}(x_1)\rangle$.

To assess finite volume effects, we consider the convolution (6) and truncate it at a distance $x_1^{\max}$. The so obtained truncated susceptibility approaches the full susceptibility at $x_1^{\max} = L/2$ and is plotted in Fig. 2 for two different volumes. On the $24^3\times 6$ lattice, the plot shows that contributions coming from the middle of the lattice volume are exponentially small, as expected. Moreover, at $x_1^{\max} = L/2$, the results obtained on the two volumes agree with each other within errors. The dominant systematic

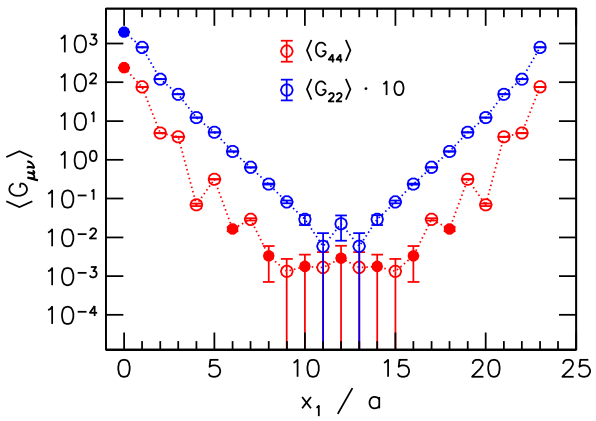

FIG. 1. Current-current $\langle G_{22}\rangle$ (blue) and density-density $\langle G_{44}\rangle$ (red) correlators at $T \approx 176$ MeV on our $24^3\times 6$ lattices. The former has been multiplied by 10 for better visibility. Filled (open) points indicate positive (negative) values.

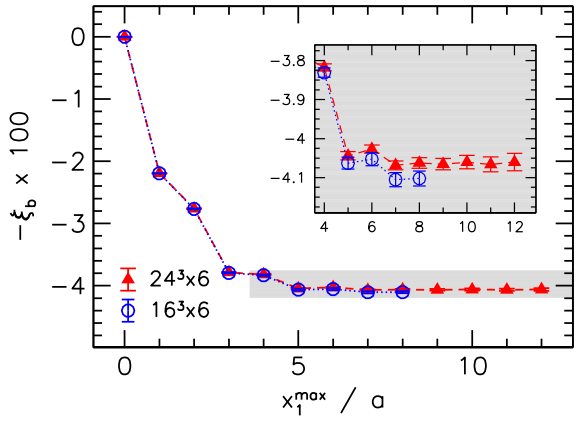

FIG. 2. Bare electric susceptibility obtained via a truncation of Eq. (6) for two different volumes, $24^3 \times 6$ (red) and $16^3 \times 6$ (blue). The inset zooms into the region near $x_1^{\max} = N_s a/2$.

error for the determination of our final result is found to come from the continuum extrapolation, which is discussed below on the level of the susceptibility ξ itself. We note that the same two-point function, $\langle G_{44} \rangle$ is required, at zero temperature, for the calculation of the hadronic contribution to the muon anomalous magnetic moment, see e.g. Ref. [55].

Once the correlator $\langle G_{44} \rangle$ is evaluated, it is convolved with the quadratic kernel according to Eq. (6) to find the bare electric susceptibility ξ_b, and its renormalization (8) is carried out by subtracting the zero-temperature contribution. The negative of the so obtained ξ is plotted in the upper panel of Fig. 3. A continuum extrapolation is performed via a multi-spline fit of all data points, taking into account $\mathcal{O}(a^2)$ lattice artefacts. The systematic error of the fit is estimated by varying the spline node points and including $\mathcal{O}(a^4)$ discretization errors in the fit at low temperatures.

For all temperatures we observe $\xi < 0$, translating to an electric permittivity below unity—a characteristic feature of plasmas [56]. At high T, our results may be compared to the high-temperature limit calculated for noninteracting quarks of mass m [12] (see also Refs. [57,58]),

$$\xi^{\text{free}} \xrightarrow{T\to\infty} -\sum_f (q_f/e)^2 \frac{N_c}{12\pi^2} \cdot \left[\log \frac{T^2\pi^2}{m^2} - 2\gamma_E - 1 \right], \qquad (19)$$

where $N_c = 3$ is the number of colors.[1] In full QCD, the quark mass is replaced by a QED renormalization scale μ_{QED} that can be determined at $T = 0$ and is found to be

[1]This formula (as well as our lattice results) correspond to the Weldon-type approach, i.e., a weak E-expansion in the infrared regularized system. Employing Schwinger's exact $E > 0$ infinite-volme propagator instead gives a perturbative result that differs from (19) by terms of $\mathcal{O}((T/m)^0)$ [12,59–61].

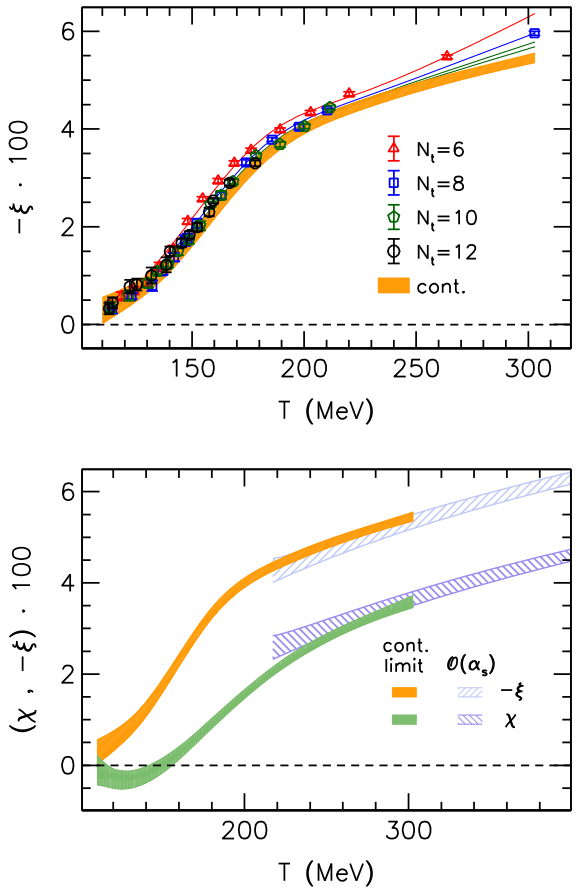

FIG. 3. Upper panel: the negative of the renormalized electric susceptibility as a function of the temperature for four lattice spacings (colored symbols) and a continuum extrapolation (orange band). Lower panel: continuum extrapolated magnetic (green) and electric (orange) susceptibilities (solid) compared to leading-order perturbation theory (dashed).

$\mu_{\text{QED}} = 115(6)$ MeV [45], close to the mass of the lightest charged hadron, i.e., the pion. Moreover, QCD corrections are included by taking into account $\mathcal{O}(\alpha_s)$ effects in the prefactor, the QED β-function [45,62]. The associated thermal scale is varied between πT and $4\pi T$ for error estimation. The so obtained curve lies very close to our results at high temperature, as visible in the lower panel of Fig. 3, where we also show the corresponding results for χ from Ref. [45].

B. Polyakov loop and the phase diagram

Next we turn to the Polyakov loop. As mentioned above, it is related to the negative exponential of the free energy of an infinitely heavy electrically neutral test quark, expected to be nonzero in the deconfined and suppressed in the confined phase. While it is only a true order parameter of deconfinement in pure gauge theory, it still acts as an approximate order parameter in full QCD and clearly signals its finite temperature crossover transition. For the

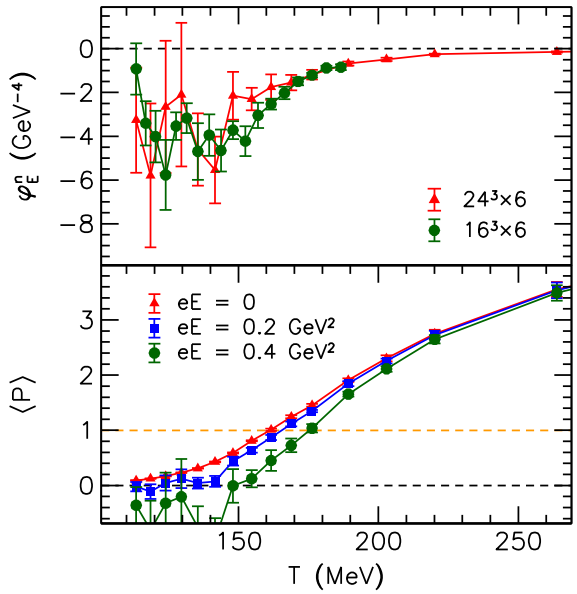

FIG. 4. Upper panel: the leading expansion coefficient of the bare Polyakov loop as a function of the temperature as obtained on two different volumes. Lower panel: renormalized Polyakov loop at nonzero electric fields, constructed from the leading Taylor series. The crossing point with the dashed yellow line is identified with T_c.

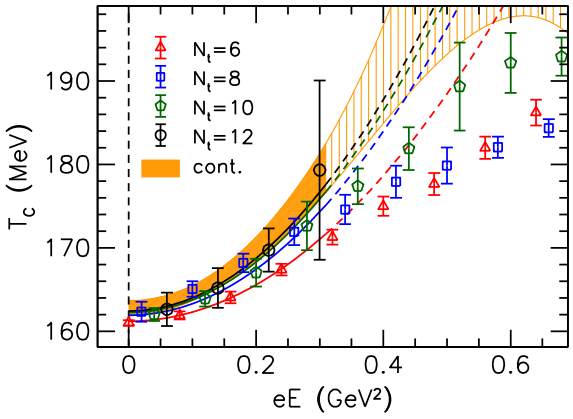

FIG. 5. Transition temperature as a function of the electric field for different lattice spacings (colored symbols) and a continuum extrapolation (yellow band). Higher-order effects in eE become non-negligible for $eE \gtrsim 0.3$ GeV^2, indicated by the dashed section of the fits.

smooth crossover many definitions of the transition temperature can be constructed, based on fermionic or gluonic observables, see, e.g., Ref. [63]. For the present study, fermionic definitions would require the measurement of three-point functions and are numerically very expensive. Therefore, here we will study the temperature and electric field dependence of the Polyakov loop and identify transition temperatures based on that.

The leading expansion of $\langle P\rangle$ with respect to the electric field is given by Eq. (10), containing the correlator of the bare observable with $-G^{(2)}_{44}$. This quantity is plotted in the upper panel of Fig. 4 for our $N_t = 6$ lattices, revealing negative values for the complete range of temperatures, i.e., a reduction of the Polyakov loop by the electric field. Finite volume effects are found to be small, although the results at low temperature have large statistical uncertainties. Using the results for the Polyakov loop at $E = 0$ [53] and the multiplicative renormalization factor from Eq. (18), we construct the E-dependence of $\langle P\rangle$, see the lower panel of Fig. 4. The Polyakov loop is known to exhibit a smooth temperature-dependence, so that a precise determination of its inflection point is cumbersome already at $E = 0$. As an alternative, we associate the transition temperature T_c with the point where $\langle P\rangle = 1$ holds. Defined in this manner, the lower panel of Fig. 4 clearly shows that T_c is increased by E. Other definitions—especially ones based on fermionic observables—will give slightly different values for the transition temperature, as expected in the case of a crossover transition. Nevertheless, as one can see from the lower panel of Fig. 4, all reasonable definitions based on the Polyakov loop will lead to an increase of the transition temperature.

Specifically, we use a piecewise linear interpolation of the $E > 0$ results for the Polyakov loop to determine the crossing point $\langle P\rangle = 1$. The statistical error is obtained via a jackknife procedure, while the systematic error is estimated by considering a cubic spline for the interpolation instead. Using the same definition for all four lattice spacings, we can construct a continuum extrapolated phase diagram based on the deconfinement temperature. We perform the continuum extrapolation by a quadratic fit of $T_c(E)$ taking into account $\mathcal{O}(a^2)$ lattice artefacts. To estimate the systematic error, we vary the fit range and also allow a quartic term in the fit. The fits are found to be stable for the region $E \lesssim 0.3$ GeV^2. To estimate the validity of our expansion, we also calculated the second derivative of $\langle P\rangle$ with respect to a background magnetic field. Comparing this leading series to existing $B > 0$ results [53], we find agreement within errors up to similar typical field strength values, $eB \lesssim 0.3$ GeV^2. Our results are shown in Fig. 5, confirming the significant enhancement of T_c as the electric field grows.

The curvature of the transition line is found to be

$$\kappa_E \equiv \left.\frac{\partial^2 T_c(E)}{\partial (eE)^2}\right|_{E=0} = 0.37(9)\ \text{GeV}^{-3}. \tag{20}$$

Furthermore, we find the transition to get stronger as E grows, revealed by an enhancement of the slope of the Polyakov loop as a function of T, see Fig. 4. However, due to the large uncertainties at low temperatures, we cannot make a quantitative statement about this aspect.

C. Imaginary electric fields

Finally, we consider lattice simulations at constant imaginary electric fields $iE = \hat{E}$. Below we will also include imaginary charge chemical potentials $i\mu = \hat{\mu}$ in the discussion. In a finite periodic volume at nonzero temperature, the allowed electric field values are quantized in terms of the smallest quark charge q_d as $q_d\hat{E} = 2\pi T/L \cdot N_e$ with the 'flux' quantum $N_e \in \mathbb{Z}$ [64]. For the down quark for example, the corresponding lattice gauge links from Sec. II read

$$u_{1,d}(x) = \begin{cases} \exp[-iaq_d\hat{E}Lx_4] & \text{if } x_1 = L-a, \\ 1 & \text{otherwise,} \end{cases}$$
$$u_{2,d}(x) = u_{3,d}(x) = 1,$$
$$u_{4,d}(x) = \exp[iaq_d\hat{E}x_1]. \tag{21}$$

This setup does not correspond to the analytic continuation of the local canonical ensemble as described in the introduction. Nevertheless, it involves a global constraint: the total electric charge in the periodic volume vanishes. As a consequence, this setup is independent of the global imaginary chemical potential. Indeed, including any $\hat{\mu} \neq 0$ can be canceled in the gauge field by a mere coordinate translation $x_1' = x_1 + \hat{\mu}/\hat{E}$. Under this change, the lattice field (21) transforms as

$$u_{4,d}(x) = \exp[iaq_d(\hat{E}x_1 + \hat{\mu})] = \exp[iaq_d\hat{E}x_1'], \tag{22}$$

which is an invariance of the system with the quantized electric field. This is in stark contrast to the situation at $\hat{E} = 0$, where a dependence on $\hat{\mu}$ is naturally present. (From this discussion it is also clear that the quantized electric field forces the independence on the chemical potential that couples to the same quantum numbers, i.e., the charge chemical potential.)

To demonstrate this point, we neglect gluonic interactions in the following. In this simplified setting, we can calculate the free energy density directly via exact diagonalization of the Dirac operator.[2] In the right side of Fig. 6 we show the results for $\Delta f = f - f(\hat{E} = \hat{\mu} = 0)$ obtained on a $200^3 \times 20$ lattice with quark mass $m/T = 0.08$. As expected, f is found to be independent of the imaginary chemical potential in the whole range $0 \leq \hat{\mu} \leq \pi T$ at any $\hat{E} \neq 0$ (the points corresponding to different $\hat{\mu}$ lie on top of each other in the figure). The comparison to a larger volume $300^3 \times 20$ shows that the smallest allowed electric field value approaches zero in the thermodynamic limit, but $\lim_{\hat{E}\to 0} f(\hat{E}) \neq f(\hat{E} = 0)$. Instead, the data points rather accumulate toward the average of f over all possible imaginary chemical potential values—i.e., a canonical setup where the total charge is constrained to zero. Altogether, we conclude that the dependence of f on $\hat{E}$ is singular at $\hat{E} = 0$ in the thermodynamic limit, rendering simulations with homogeneous imaginary electric fields unsuited for the evaluation of ξ.

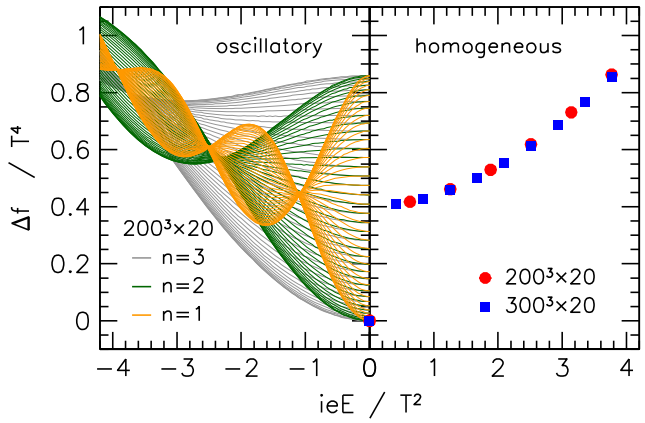

FIG. 6. Free energy density as a function of homogeneous (right side) and oscillatory (left side) imaginary electric fields. The results for different imaginary chemical potentials correspond to the set of curves in the left ($\hat{\mu}$ grows from 0 to πT from the bottom to the top), while they lie on top of each other on the right.

In addition, the left side of Fig. 6 shows Δf for oscillatory imaginary electric fields with the profile $\hat{E}(x_1) = \hat{E}\sqrt{2}\cos(2\pi n x_1/L)$. In this case, only the $u_{4,f}(x)$ lattice links are nontrivial. The role of the infrared regulator is played by the wave number n and not by the volume. Moreover, here $\hat{E}$ is a continuous variable but $n \in \mathbb{Z}$ is discrete. This setup does not fix the overall charge and, therefore, maintains the dependence of f on $\hat{\mu}$. Indeed, the results reveal a continuous behavior as a function of $\hat{E}$ and $\hat{\mu}$. However, as visible in the plot, the results again approach a singular behavior as the infrared regulator is removed: the curves collapse to a set of node-points, independent of $\hat{\mu}$, approaching the $\hat{E} = 0$ axis. In particular, by looking at the behavior of the $\hat{\mu} = 0$ curves near $\hat{E} = 0$, one sees that the curvature of f with respect to $\hat{E}$ diverges for $n \to 0$. Thus, the homogeneous limit of the setup with oscillatory imaginary fields reproduces what we have already seen for the homogeneous case.

In the interacting case, the dependence of the Polyakov loop on $\hat{E}$ reinforces this picture. In lattice simulations with constant imaginary electric fields at nonzero temperature, the Polyakov loop was observed to develop a local phase proportional to the local vector potential $\arg P_b(x_1) \propto e\hat{E}x_1/T$ [33] (see also the analogous study [65]). This results from the preference of local Polyakov loops toward different center sectors for different x_1. Together with the quantization condition for the imaginary electric flux, this corresponds to a topological behavior of the Polyakov loop angle winding around the lattice. Thus, the volume-averaged

[2]Some of the results in Fig. 6 we discussed previously in Ref. [12].

P_b vanishes in these simulations, showing the singular change of relevant ensembles as the electric field is switched on (grand canonical at $\hat{E} = 0$ but canonical at $\hat{E} > 0$). Again, we conclude that simulations with homogeneous imaginary electric fields cannot be used for a direct comparison to the $\hat{E} = 0$ system.

IV. DISCUSSION

In this paper we studied the thermodynamics of QCD at nonzero background electric fields E via lattice simulations with physical quark masses. To avoid the complex action problem at $E > 0$, we employed a leading-order Taylor-expansion. This approach is more complicated than the analogous expansion in a chemical potential, because the impact of E on the equilibrium charge distribution needs to be taken into account [12]. Our results, measured on four different lattice spacings and extrapolated to the continuum limit, demonstrate two main effects. First, that QCD matter is described by a negative electric susceptibility at all temperatures. Second, that the QCD transition, as defined in terms of the Polyakov loop, is shifted to higher temperatures as the electric field grows, leading to the phase diagram in Fig. 5. Furthermore, we showed that lattice simulations employing imaginary electric fields cannot be used to directly assess these aspects due to a singular behavior around $E = 0$.

We mention that the susceptibility and the phase diagram are both encoded by the thermal contributions to the real part of the free energy density. These are therefore not impacted by Schwinger pair creation, which is related to the imaginary part of f and is known to be independent of the temperature [59,60]. In other words, the equilibrium charge profile and the polarization of the medium are related to the distribution of thermal charges and not of those created from the vacuum via the Schwinger effect.

Finally we point out that calculations within the PNJL model [40], employing the Schwinger propagator, predict the opposite picture for the phase diagram as compared to our findings. Whether the same tendency holds for the Weldon-type regularization within this model, is an open question calling for further study. Besides this aspect, the PNJL model is known to miss important gluonic effects in the presence of electromagnetic fields and fails to correctly describe the phase diagram at $B > 0$ [23]. It would be interesting to see whether improvements that were found to correct these shortcomings of the model in the magnetic setting [66] also work in the $E > 0$ case.

ACKNOWLEDGMENTS

This research was funded by the DFG (SFB TRR 211—project number 315477589). The authors are grateful to Andrei Alexandru, Bastian Brandt, David Dudal, Duifje van Egmond, and Urko Reinosa for enlightening discussions.

[1] D. Kharzeev, K. Landsteiner, A. Schmitt, and H.-U. Yee, Strongly interacting matter in magnetic fields, Lect. Notes Phys. **871**, 1 (2013).
[2] V. A. Miransky and I. A. Shovkovy, Quantum field theory in a magnetic field: From quantum chromodynamics to graphene and Dirac semimetals, Phys. Rep. **576**, 1 (2015).
[3] A. Schmitt, Chiral pasta: Mixed phases at the chiral phase transition, Phys. Rev. D **101**, 074007 (2020).
[4] W.-T. Deng and X.-G. Huang, Electric fields and chiral magnetic effect in Cu + Au collisions, Phys. Lett. B **742**, 296 (2015).
[5] V. Voronyuk, V. D. Toneev, S. A. Voloshin, and W. Cassing, Charge-dependent directed flow in asymmetric nuclear collisions, Phys. Rev. C **90**, 064903 (2014).
[6] K. Tuchin, Time and space dependence of electromagnetic field in relativistic heavy-ion collisions, Phys. Rev. C **88**, 024911 (2013).
[7] L. McLerran and V. Skokov, Comments about the electromagnetic field in heavy-ion collisions, Nucl. Phys. **A929**, 184 (2014).
[8] X.-G. Huang, Electromagnetic fields and anomalous transports in heavy-ion collisions—A pedagogical review, Rep. Prog. Phys. **79**, 076302 (2016).
[9] H. B. Meyer, Transport properties of the quark-gluon plasma: A lattice QCD perspective, Eur. Phys. J. A **47**, 86 (2011).
[10] L. Landau and E. Lifshitz, *Statistical Physics: Volume 5. No. Bd. 5* (Elsevier Science, New York, 2013).
[11] J. M. Luttinger, Theory of thermal transport coefficients, Phys. Rev. **135**, A1505 (1964).
[12] G. Endrődi and G. Markó, On electric fields in hot QCD: Perturbation theory, J. High Energy Phys. 12 (2022) 015.
[13] J. S. Schwinger, On gauge invariance and vacuum polarization, Phys. Rev. **82**, 664 (1951).
[14] H. A. Weldon, Covariant calculations at finite temperature: The relativistic plasma, Phys. Rev. D **26**, 1394 (1982).
[15] Y. Aoki, G. Endrődi, Z. Fodor, S. Katz, and K. Szabó, The order of the quantum chromodynamics transition predicted by the standard model of particle physics, Nature (London) **443**, 675 (2006).
[16] T. Bhattacharya, M. I. Buchoff, N. H. Christ, H.-T. Ding, R. Gupta *et al.*, QCD phase transition with chiral quarks and physical quark masses, Phys. Rev. Lett. **113**, 082001 (2014).
[17] M. D'Elia, S. Mukherjee, and F. Sanfilippo, QCD phase transition in a strong magnetic background, Phys. Rev. D **82**, 051501 (2010).

[18] G. Bali, F. Bruckmann, G. Endrődi, Z. Fodor, S. Katz, S. Krieg, A. Schäfer, and K. K. Szabó, The QCD phase diagram for external magnetic fields, J. High Energy Phys. 02 (2012) 044.
[19] G. Bali, F. Bruckmann, G. Endrődi, Z. Fodor, S. Katz, and A. Schäfer, QCD quark condensate in external magnetic fields, Phys. Rev. D **86**, 071502 (2012).
[20] G. Endrődi, Critical point in the QCD phase diagram for extremely strong background magnetic fields, J. High Energy Phys. 07 (2015) 173.
[21] M. D'Elia, L. Maio, F. Sanfilippo, and A. Stanzione, Phase diagram of QCD in a magnetic background, Phys. Rev. D **105**, 034511 (2022).
[22] B. B. Brandt, F. Cuteri, G. Endrődi, G. Markó, L. Sandbote, and A. D. M. Valois, Thermal QCD in a non-uniform magnetic background, J. High Energy Phys. 11 (2023) 229.
[23] J. O. Andersen, W. R. Naylor, and A. Tranberg, Phase diagram of QCD in a magnetic field: A review, Rev. Mod. Phys. **88**, 025001 (2016).
[24] H. R. Fiebig, W. Wilcox, and R. M. Woloshyn, A study of hadron electric polarizability in quenched lattice QCD, Nucl. Phys. **B324**, 47 (1989).
[25] J. C. Christensen, W. Wilcox, F. X. Lee, and L.-m. Zhou, Electric polarizability of neutral hadrons from lattice QCD, Phys. Rev. D **72**, 034503 (2005).
[26] M. Engelhardt (LHPC Collaboration), Neutron electric polarizability from unquenched lattice QCD using the background field approach, Phys. Rev. D **76**, 114502 (2007).
[27] F. X. Lee, A. Alexandru, C. Culver, and W. Wilcox, Charged pion electric polarizability from four-point functions in lattice QCD, Phys. Rev. D **108**, 014512 (2023).
[28] W. Detmold, B. C. Tiburzi, and A. Walker-Loud, Extracting electric polarizabilities from lattice QCD, Phys. Rev. D **79**, 094505 (2009).
[29] W. Detmold, B. C. Tiburzi, and A. Walker-Loud, Extracting nucleon magnetic moments and electric polarizabilities from lattice QCD in background electric fields, Phys. Rev. D **81**, 054502 (2010).
[30] M. Lujan, A. Alexandru, W. Freeman, and F. Lee, Electric polarizability of neutral hadrons from dynamical lattice QCD ensembles, Phys. Rev. D **89**, 074506 (2014).
[31] W. Freeman, A. Alexandru, M. Lujan, and F. X. Lee, Sea quark contributions to the electric polarizability of hadrons, Phys. Rev. D **90**, 054507 (2014).
[32] M. Lujan, A. Alexandru, W. Freeman, and F. X. Lee, Finite volume effects on the electric polarizability of neutral hadrons in lattice QCD, Phys. Rev. D **94**, 074506 (2016).
[33] J.-C. Yang, X.-T. Chang, and J.-X. Chen, Study of the Roberge-Weiss phase caused by external uniform classical electric field using lattice QCD approach, J. High Energy Phys. 10 (2022) 053.
[34] B. Brandt, F. Cuteri, G. Endrődi, J. J. H. Hernández, and G. Markó, QCD topology with electromagnetic fields and the axion-photon coupling, Proc. Sci. LATTICE2022 (**2023**) 174.
[35] J.-C. Yang, X. Zhang, and J.-X. Chen, Study of the effects of external imaginary electric field and chiral chemical potential on quark matter, arXiv:2309.09281.
[36] A. Yamamoto, Lattice QCD with strong external electric fields, Phys. Rev. Lett. **110**, 112001 (2013).
[37] H. Suganuma and T. Tatsumi, On the behavior of symmetry and phase transitions in a strong electromagnetic field, Ann. Phys. (N.Y.) **208**, 470 (1991).
[38] S. Klevansky and R. H. Lemmer, Chiral symmetry restoration in the Nambu-Jona-Lasinio model with a constant electromagnetic field, Phys. Rev. D **39**, 3478 (1989).
[39] A. Yu. Babansky, E. V. Gorbar, and G. V. Shchepanyuk, Chiral symmetry breaking in the Nambu-Jona-Lasinio model in external constant electromagnetic field, Phys. Lett. B **419**, 272 (1998).
[40] W. R. Tavares, R. L. S. Farias, and S. S. Avancini, Deconfinement and chiral phase transitions in quark matter with a strong electric field, Phys. Rev. D **101**, 016017 (2020).
[41] W. R. Tavares, S. S. Avancini, and R. L. S. Farias, Quark matter under strong electric fields in the linear sigma model coupled with quarks, Phys. Rev. D **108**, 016017 (2023).
[42] S. Ozaki, T. Arai, K. Hattori, and K. Itakura, Euler-Heisenberg-Weiss action for QCD + QED, Phys. Rev. D **92**, 016002 (2015).
[43] G. Endrődi and G. Markó, Thermal QCD with external imaginary electric fields on the lattice, Proc. Sci. LATTICE2021 (**2022**) 245.
[44] G. Bali and G. Endrődi, Hadronic vacuum polarization and muon g-2 from magnetic susceptibilities on the lattice, Phys. Rev. D **92**, 054506 (2015).
[45] G. S. Bali, G. Endrődi, and S. Piemonte, Magnetic susceptibility of QCD matter and its decomposition from the lattice, J. High Energy Phys. 07 (2020) 183.
[46] P. V. Buividovich, D. Smith, and L. von Smekal, Static magnetic susceptibility in finite-density $SU(2)$ lattice gauge theory, Eur. Phys. J. A **57**, 293 (2021).
[47] S. Borsányi, G. Endrődi, Z. Fodor, A. Jakovác, S. D. Katz, S. Krieg, C. Ratti, and K. K. Szabó, The QCD equation of state with dynamical quarks, J. High Energy Phys. 11 (2010) 077.
[48] Y. Aoki, Z. Fodor, S. Katz, and K. Szabó, The equation of state in lattice QCD: With physical quark masses towards the continuum limit, J. High Energy Phys. 01 (2006) 089.
[49] C. Bonati, M. D'Elia, M. Mariti, F. Negro, and F. Sanfilippo, Magnetic susceptibility and equation of state of $N_f = 2 + 1$ QCD with physical quark masses, Phys. Rev. D **89**, 054506 (2014).
[50] G. V. Dunne, Heisenberg-Euler effective Lagrangians: Basics and extensions, arXiv:hep-th/0406216.
[51] G. Bali, F. Bruckmann, G. Endrődi, S. Katz, and A. Schäfer, The QCD equation of state in background magnetic fields, J. High Energy Phys. 08 (2014) 177.
[52] S. Borsányi, S. Dürr, Z. Fodor, C. Hoelbling, S. D. Katz, S. Krieg, D. Nógrádi, K. K. Szabó, B. C. Tóth, and Norbert Trombitás, QCD thermodynamics with continuum extrapolated Wilson fermions I, J. High Energy Phys. 08 (2012) 126.
[53] F. Bruckmann, G. Endrődi, and T. G. Kovács, Inverse magnetic catalysis and the Polyakov loop, J. High Energy Phys. 04 (2013) 112.
[54] R. Bellwied, S. Borsanyi, Z. Fodor, S. D. Katz, and C. Ratti, Is there a flavor hierarchy in the deconfinement transition of QCD?, Phys. Rev. Lett. **111**, 202302 (2013).

[55] H. B. Meyer and H. Wittig, Lattice QCD and the anomalous magnetic moment of the muon, Prog. Part. Nucl. Phys. **104**, 46 (2019).
[56] J. D. Jackson, *Classical Electrodynamics*, 3rd ed. (Wiley, New York, NY, 1999), http://cdsweb.cern.ch/record/490457.
[57] S. Carignano, C. Manuel, and J. Soto, Power corrections to the HTL effective Lagrangian of QED, Phys. Lett. B **780**, 308 (2018).
[58] O. Ferreira and E. S. Fraga, Power corrections to the photon polarization tensor in a hot and dense medium of massive fermions, arXiv:2309.06524.
[59] P. Elmfors and B.-S. Skagerstam, Electromagnetic fields in a thermal background, Phys. Lett. B **348**, 141 (1995); **376**, 330(E) (1996).
[60] H. Gies, QED effective action at finite temperature, Phys. Rev. D **60**, 105002 (1999).
[61] H. Gies, Light cone condition for a thermalized QED vacuum, Phys. Rev. D **60**, 105033 (1999).
[62] P. A. Baikov, K. G. Chetyrkin, and J. H. Kühn, Five-loop running of the QCD coupling constant, Phys. Rev. Lett. **118**, 082002 (2017).
[63] S. Borsányi, Z. Fodor, C. Hoelbling, S. D. Katz, S. Krieg, C. Ratti, and K. K. Szabó (Wuppertal-Budapest Collaboration), Is there still any T_c mystery in lattice QCD? Results with physical masses in the continuum limit III, J. High Energy Phys. 09 (2010) 073.
[64] G. 't Hooft, A property of electric and magnetic flux in nonabelian gauge theories, Nucl. Phys. **B153**, 141 (1979).
[65] M. D'Elia and M. Mariti, Effect of compactified dimensions and background magnetic fields on the phase structure of SU(N) gauge theories, Phys. Rev. Lett. **118**, 172001 (2017).
[66] G. Endrődi and G. Markó, Magnetized baryons and the QCD phase diagram: NJL model meets the lattice, J. High Energy Phys. 08 (2019) 036.